The recruitment of ACF1 and SMARCA5 to DNA lesions relies on ADP-ribosylation dependent chromatin unfolding

Eva Pinto Jurado, Rebecca Smith, Nicolas Bigot, Catherine Chapuis, Gyula Timinszky, Sébastien Huet

The recruitment of ACF1 and SMARCA5 to DNA lesions relies on ADP-ribosylation dependent chromatin unfolding

Eva Pinto Jurado[1,2,3,*], Rebecca Smith[1,*,#,†], Nicolas Bigot[1], Catherine Chapuis[1], Gyula Timinszky[2,#] and Sébastien Huet[1,4,#].

1 Univ Rennes, CNRS, IGDR (Institut de génétique et développement de Rennes) - UMR 6290, BIOSIT – UMS3480, F- 35000 Rennes, France
2 Laboratory of DNA Damage and Nuclear Dynamics, Institute of Genetics, Biological Research Centre, Eötvös Loránd Research Network (ELKH), Szeged, Hungary
3 Doctoral School of Multidisciplinary Medical Sciences, University of Szeged, Szeged, Hungary
4 Institut Universitaire de France, F-75000 Paris, France

*equal contributions
[#]Correspondence to: R.S. (rebecca.smith@path.ox.ac.uk), G.T. (timinszky.gyula@brc.hu), or S.H. (sebastien.huet@univ-rennes.fr)
[†]Present address: Sir William Dunn School of Pathology, University of Oxford, South Parks Road, Oxford, OX1 3RE, UK.

Number of characters: 20355

ABSTRACT

ADP-ribosylation signaling orchestrates the recruitment of various repair actors and chromatin remodeling processes promoting access to lesions during the early stages of the DNA damage response. The chromatin remodeler complex ACF, composed of the ATPase subunit SMARCA5/SNF2H and the cofactor ACF1/BAZ1A, is among the factors that accumulate at DNA lesions in an ADP-ribosylation dependent manner. In this work, we show that each subunit of the ACF complex accumulates to DNA breaks independently from its partner. Furthermore, we demonstrate that the recruitment of SMARCA5 and ACF1 to sites of damage is not due to direct binding to the ADP-ribose moieties but to facilitated DNA binding at relaxed ADP-ribosylated chromatin. Therefore, our work provides new insights regarding the mechanisms underlying the timely accumulation of ACF1 and SMARCA5 to DNA lesions, where they contribute to efficient DNA damage resolution.

INTRODUCTION

Several chromatin remodelers recruit early to lesions during the DNA damage response (DDR), facilitating efficient double-strand break (DSB) repair *via* homologous recombination and non-homologous end-joining pathways (Lan et al., 2010; Polo et al., 2010; Luijsterburg et al., 2016). These remodelers participate in various steps including altering chromatin architecture for repair machinery access (Xu et al., 2010; Smeenk et al., 2013; Smith et al., 2018), inhibiting interfering processes like transcription (Gong et al., 2015), and scaffolding core repair factors (Lan et al., 2010).

The accumulation of many of these remodeling complexes is regulated by the ADP-ribosylation signaling pathway, which is among the first one to be activated upon DNA damage (Liu et al., 2017). This pathway relies mainly on the activity of PARP1, the founding member of the PARP family (Suskiewicz et al., 2023). PARP1 directly binds single and double strand breaks, which triggers its catalytic activity *via* a complex allosteric mechanism (Langelier et al., 2012). PARP1 catalyzes the addition of ADP-ribose (ADPr) moieties onto specific residues on itself, core and linker histones and nearby proteins and extends mono-ADPr moieties to form poly-ADPr chains (Longarini et al., 2023). Some chromatin remodelers, such as ALC1/CHD1L and CHD2 directly bind these ADPr marks *via* dedicated domains (Luijsterburg et al., 2016; Singh et al., 2017). Alternatively, increased DNA accessibility at unfolded ADP-ribosylated chromatin contributes to the recruitment of remodelers such as CHD4 and CHD7 (Smith et al., 2018; Rother et al., 2020).

In the current work, we further investigated the mechanism enabling the timely accumulation of the ACF complex at DNA lesions. This complex between the SMARCA5 ATPase and ACF1 regulatory subunit (Ito et al., 1999; Erdel et al., 2010) facilitates double-strand break repair through chromatin remodeling and stabilization of core factors like Ku70/80 and RNF168 at sites of damage (Lan et al., 2010; Smeenk et al., 2013; Klement et al., 2014). We find that ACF1 and SMARCA5 independently recruit to DNA lesions. Moreover, their ADPr-dependent accumulation does not involve direct ADPr binding but rather depends on enhanced accessibility to DNA lesions at relaxed ADP-ribosylated chromatin.

RESULTS AND DISCUSSION

Both subunits of the ACF complex accumulate at DNA lesions independently of each other

The ACF chromatin remodeler complex subunits have been reported to accumulate quickly at sites of DNA damage induced using various methods (Lan et al., 2010; Erdel et al., 2010; Smeenk et al., 2013). In line with these previous findings, we found that fluorescently tagged SMARCA5 and ACF1 recruited efficiently to sites of DNA damage induced by 405 nm laser irradiation of U2OS cells presensitized with Hoechst (Figure 1,A and B). Previous reports analyzing the behavior of mutants missing specific domains crucial for complex formation proposed that the accumulation of ACF1 to DNA lesions relies on its interaction with SMARCA5 and *vice-versa* (Lan et al., 2010; Sánchez-Molina et al., 2011). Nevertheless, since the domains studied could mediate interactions with other factors and DNA, we aimed to investigate the interdependency of the recruitment of the two subunits more directly by analyzing their accumulation kinetics upon depletion of each subunit. We found that SMARCA5 knockdown (KD) did not significantly impact ACF1 recruitment (Figure 1, C-E) and, conversely, ACF1 KD did not alter SMARCA5 accumulation to sites of damage (Figure 1, F and G). Longer time-lapses revealed a slightly premature release of ACF1 upon SMARCA5 KD while depleting ACF1 had no impact on the recruitment kinetics of SMARCA5 (Figure S1). Therefore, our findings suggest that while both subunits accumulate independently at sites of damage, the stabilization of ACF1 on the DNA lesions requires the presence of SMARCA5.

Recruitment of ACF1 and SMARCA5 to DNA lesions is promoted by ADP-ribose-dependent unfolding of chromatin

Aligning with other remodelers facilitating DNA repair and in agreement with previous reports (Lan et al., 2010; Smeenk et al., 2013; Luijsterburg et al., 2016; Sellou et al., 2016; Rother et al., 2020), we observed strongly impaired accumulation of both endogenous and GFP-tagged ACF1 and SMARCA5 at damage sites upon PARP inhibitor (PARPi) treatment (Figure 2, A and B; Figure S2, A and B). This implies ADPr dependence irrespective of protein overexpression or tagging.

Immunoprecipitating YFP-tagged PARP1 revealed an interaction with SMARCA5 independently of DNA damage or PARP inhibition (Figure S2, C). Since PARP1 is recruited

to damage even in the presence of PARPi (Prokhorova et al., 2021), this constitutive interaction between PARP1 and SMARCA5 could trigger the slight accumulation of SMARCA5 at DNA lesions in PARPi treated cells. However, it does not account for the strong dependency of SMARCA5 recruitment to PARPi. To investigate this question further, we tested the possibility that ACF1 and SMARCA5 bind ADPr in living cells, which could trigger their rapid accumulation to damage. First we co-expressed a fusion between the Lac repressor and a GFP nanobody, GFP-tagged ACF1 or SMARCA5, and mCherry-tagged PARP1 in U2OS cells bearing a Lac operator array in their genome. With this set-up, the cluster of GFP-tagged ACF1 or SMARCA5 at the Lac operator (LacO) array was used as a bait, while mCherry PARP1 was the prey (Smith et al., 2018). After microirradiation away from the LacO array, PARP1 is quickly ADP-ribosylated and released from the sites of damage, diffusing through the nucleus in an ADP-ribosylated state. While a well-known ADPr-binding bait such as GFP-tagged macrodomain of macroH2A1.1 (Timinszky et al., 2009), was able to efficiently capture ADP-ribosylated PARP1, leading to increased mCherry signal at the LacO array (Figure S2, D and E), ACF1 and SMARCA5 both failed to do so, indicating that they are unable to interact with ADPr (Figure 2, C-F). To confirm this result with an alternative approach, we assessed the impact on protein recruitment of an acute PARP inhibitor treatment 3 min post-irradiation (Smith et al., 2019). Because ADPr shows high turnover at DNA lesions due to the opposite activities of PARP1 and poly(ADP-ribose) glycosylase, PARP inhibitor treatment post-irradiation led to a rapid decrease in ADPr at DNA lesions, as seen by the dissipation of the WWE domain of RNF146, known to display strong affinity for ADPr (Zhang et al., 2011) (Figure S2, F and G). In contrast, PARP inhibitor added post-irradiation had no impact on the accumulation of either ACF1 or SMARCA5. This finding, together with the previous assay, argues against a recruitment of ACF1 and SMARCA5 to sites of DNA damage due to an interaction with ADPr (Figure 2, G-J).

As our data show ACF1 and SMARCA5 lack ADPr binding, their accumulation to DNA lesions could rely on ADPr-dependent chromatin unfolding, a mechanism driving the recruitment of several other repair factors (Smith et al., 2019; Smith et al., 2023). We tested this hypothesis by analyzing the recruitment of both subunits in cells overexpressing the chromatin remodeler ALC1, which stimulates chromatin unfolding without affecting ADPr signaling at DNA lesions (Sellou et al., 2016). We controlled wild-type and catalytically dead ALC1-K77R ALC1 impact on damage-induced chromatin relaxation by quantifying the thickness of a photoactivated H2B-PATagRFP chromatin stripe generated simultaneously to

damage induction (Sellou et al., 2016) (Figure 3, A). In agreement with previous findings, overexpressing wild-type ALC1 led to a dramatic increase in chromatin relaxation compared to cells expressing ALC1-K77R (Figure 3, B). We also observed that enhanced chromatin relaxation upon wild-type ALC1 overexpression correlated with stronger ACF1 (Figure 3, C and D) and SMARCA5 (Figure 3, E and F) accumulation to DNA damage. This increased recruitment was lost in cells treated with PARPi (Figure S3), in line with the ADPr-dependent recruitment of ALC1 to the lesions (Sellou et al., 2016). Based on all these results, we conclude that while interaction with PARP1 may enable modest recruitment of ACF1 and SMARCA5, it is the ADPr-mediated chromatin unfolding proximal to lesions that predominantly triggers ACF1 and SMARCA5 accumulation to DNA lesions.

Accumulation of ACF1 and SMARCA5 to DNA lesions relies on their ability to bind DNA

We previously demonstrated that ADPr-triggered remodeling that occurs upon DNA damage yields a transient open chromatin conformation with increased DNA exposure but unaltered nucleosome accessibility (Smith et al., 2019). Since such remodeling enhances ACF1/SMARCA5 recruitment, we examined how their affinity for DNA could impact their recruitment to DNA lesions.

ACF1 can be divided into three main parts. The N-terminal region (4-309 a.a.) has been shown to mediate DNA binding of the ACF complex *in vitro* (Fyodorov et al., 2002) (Figure 4A). The middle region of ACF1 (312-1061 a.a.) bears the DDT and BAZ motifs triggering association with SMARCA5 (Fyodorov et al., 2002). Finally, the C-terminus of ACF1 (1062-1557 a.a.) contains PHD and BRD motifs regulating histone binding (Eberharter et al. 2004). We focused on ACF1 domains involved in DNA binding and aimed to correlate ACF1 affinity for DNA with its accumulation at DNA lesions. We subdivided the N-terminal region into two domains: the WAC motif (4-111 a.a) and a second poorly-characterized region (154-309 a.a), previously identified as mediating binding to DNA *in vitro* (Fyodorov et al., 2002), which we refer to as DNA-binding domain 2 (DBD2). We previously demonstrated, by using fluorescence correlation spectroscopy (FCS), that DNA binding affinity inversely correlates with nuclear diffusion speed (Smith et al., 2019). The fast decrease of the FCS autocorrelation curve obtained for the ΔWAC construct compared to wild-type ACF1 was indicative of an increase in diffusion speed due to lower association with DNA (Figure 4B). The DBD2 domain deletion had an even stronger impact on protein diffusion, which was not further

enhanced by the truncation of WAC and DBD2, indicating that DBD2 dominantly governs this DNA binding. Accordingly, by analyzing the behavior of the ACF1 truncation mutants at sites of DNA lesions, we found the DBD2 deletion severely impaired ACF1 accumulation at laser damage sites while WAC truncation had milder effects (Figure 4, C and D). We also observed that the DBD2 domain alone, but not the WAC, accumulated rapidly at sites of DNA damage (Figure 4, E and F) but was unable to maintain a sustained accumulation, in association or not with WAC, and rapidly dissipated from the sites of damage unlike the full-length ACF1. We wondered whether this stabilization of full-length ACF1 could rely on interactions with histones via the PHD and BRD domains. However, a mutant lacking these two domains showed similar recruitment compared to full-length ACF1, arguing against this possibility (Figure S4). Together with our observations that SMARCA5 knockdown hastened ACF1 release (Figure S1, A-C), these findings draw a model in which the initial accumulation of ACF1 at sites of damage is triggered by DNA binding *via* the WAC and DBD2 domains, while stabilization in this area relies on ACF1 interaction with SMARCA5 *via* the DDT/BAZ domains.

SMARCA5 possess an N-terminal ATPase domain (1-673 a.a.) and a C-terminal half (674-1051 a.a.) that drives substrate recognition through three conserved sub-domains: HAND, SANT and SLIDE, the latter being crucial for DNA interaction at the nucleosome based on previous *in vitro* findings (Grüne et al., 2003). Using FCS, we found that a ΔSLIDE mutant, in contrast to the ΔHAND or the ΔSANT constructs, displayed increased diffusivity compared to wild-type SMARCA5, indicative of reduced DNA affinity (Figure 4G). SLIDE truncation dramatically impaired SMARCA5 recruitment to laser damage while ΔHAND and ΔSANT behaved similar to wild-type, mirroring their DNA binding capacities (Figure 4, H and I), in agreement with previous findings (Lan et al., 2010). Therefore, similar to what we observed for ACF1, SMARCA5 accumulation at DNA lesion correlated with DNA binding affinity.

Together with our previous reports (Smith et al., 2019, Smith et al., 2023), our current results highlight ADPr-mediated chromatin unfolding and enhanced DNA access as a common mechanism promoting DNA repair factors accrual. This mechanism appears very generic as it would trigger the accumulation of any nuclear factor showing DNA-binding ability, including transcription factors not necessarily linked to DNA repair (Izhar et al., 2015). Therefore, recruitment is likely followed by filtering step consisting of the selective stabilization of repair factors in the damaged region while other proteins get quickly mobilized. This could involve binding to specific histones or post-translational marks, as shown for example for

ZMYM3 (Leung et al., 2017), or formation of complexes, as we propose here for ACF1, which association with SMARCA5 contributes to its maintenance at DNA lesions.

The ACF complex does not contribute to chromatin remodeling at early stage of the DDR.

Previous work reported that the ACF complex triggers heterochromatin unfolding upon DNA damage (Klement et al., 2014). We wondered whether this remodeling activity could promote a local open state independently of the chromatin landscape. However, KD of SMARCA5, the catalytic subunit of the ACF complex, had no impact on chromatin unfolding (Figure 5). Given that our irradiation method mainly damages the more central euchromatin rather than peripheral heterochromatin, these findings suggest no contribution of the ACF complex to euchromatin relaxation, in contrast to heterochromatin. In the former regions, ACF1 and SMARCA5 could rather act as scaffold for the core repair actors Ku70/80 and RNF168 (Lan et al., 2010, Smeenk et al., 2013). We recently reported that the recruitment of ZNF384 and ZMYM3, two adaptor proteins promoting the stabilization of NHEJ and HR factors at the lesions (Leung et al., 2017, Singh et al., 2021), was promoted by ADPr-dependent chromatin unfolding (Smith et al., 2023). Therefore, this early DDR step might contribute to create a local environment favoring not only the recruitment of the repair actors but also their stabilization at the DNA lesions prior to the repair pathway choice.
It should be noted that our work focused on the behavior of the ACF complex after laser irradiation, which allows for a precise characterization of protein dynamics and chromatin remodeling at sites of damage but generates a mixture of DNA lesions (Kong et al., 2009). Therefore, future work using alternative DNA damaging methods will be needed to further delineate the exact contribution of the ACF complex to specific repair pathways.

MATERIAL AND METHODS

Plasmids and siRNA

Plasmids encoding PATagRFP-H2B (Sellou et al., 2016), GFP-WWE (from RNF146) (Sellou et al., 2016), mCherry-PARP1 (Juhász et al., 2020), YFP-macroH2A1.1 macrodomain (Timinszky et al., 2009), GFP nanobody-LacI fusion (Smith et al., 2018) and iRFP670-ALC1 (WT) (Smith et al., 2018) were described previously. iRFP670-ALC1 K77R was made by exchanging mCherry from mCherry-ALC1 K77R (Sellou et al., 2016) with iRFP670 from

iRFP670-ALC1 WT using *Age*I and *BsRG*I restriction enzymes. SMARCA5-EGFP, RFP-SMARCA5 and ACF1-GFP were kind gifts from K.Rippe (Erdel et al., 2010). SMARCA5ΔHAND-EGFP, SMARCA5ΔSANT-EGFP, SMARCA5ΔSLIDE-EGFP were a kind gift from H.Lans (Aydin et al., 2014). The individual domains of ACF1, WAC (1-140 a.a), DBD2 (141-400 a.a), WAC-DBD2 (1-400 a.a) were cloned into pEGFP-N1 with primers described in table S1. ACF1 deletion mutants ACF1ΔWAC-EGFP, ACF1ΔDBD2-EGFP and ACF1-ΔWACΔDBD2-EGFP were cloned into pEGFP-N1 using Gibson assembly with the primers described in Table S1 from ACF1-eGFP. ACF1-ΔC-EGFP (1-1147 a.a) was made by cloning a PCR fragment with the primers described in Table S1 from ACF1-eGFP into pEGFP-N1 digested by BamHI and KpnI (Thermo). Silencer Select siRNA (Thermo Scientific) were used for siRNA-mediated knockdown of target proteins (siACF1-1 #S22059, siACF1-2 #s22060 siSMARCA5-1 #s16081, siSMARCA5-2 #s16082, siCTRL #4390846).

Cell culture, Hoechst presensitization and PARP inhibition

Parental U2OS cells were obtained from ATCC. These cells are not among the database of commonly misidentified cell lines. All cultured cell lines were checked for mycoplasma every 3 months and upon suspicion of contamination. Wild-type U2OS, U2OS 2B2 (Czarna et al., 2013), U2OS PAGFP-H2B expressing cells (Smith et al., 2018) and U2OS Flp-In T-REx YFP-tagged-PARP1 (Prokhorova et al., 2021) cells were cultured in DMEM (4.5 g/l glucose, Sigma) supplemented with 10% fetal bovine serum (Life Technologies), 2 mM glutamine (Sigma), 100 µg/ml penicillin and 100 U/ml streptomycin (Sigma) in a humidified incubator at 37◦C with 5% CO2. For transient expression of plasmids, cells were transfected 12–24 h after seeding into eight-well Imaging Chamber CG (Zell-Kontakt) with XtremeGENE HP (Sigma) or Xfect (Clontech) according to the manufacturer's instructions and incubated for 48 h prior to imaging. For Hoechst presensitization, growth medium was aspirated from the LabTek and replaced with fresh medium containing 0.3 µg/ml Hoechst 33342 for 1 h at 37◦C. Immediately prior to imaging, growth medium was replaced with CO_2-independent imaging medium (Phenol Red-free Leibovitz's L-15 medium (Life Technologies) supplemented with 20% fetal bovine serum, 100 µg/ml penicillin and 100 U/ml streptomycin). For PARP inhibition, cells were treated with 30 µM Olaparib (Euromedex) for 30 min prior to imaging or 3 min after micro-irradiations. All experiments were completed with unsynchronized cells. For siRNA-mediated knockdown, cells were transfected with 2 pmol of siRNA per well of an 8-well Imaging Chamber using Lipofectamine RNAiMAX (Invitrogen) according to the manufactures instructions and incubated for 24 h prior to plasmid transfection as described

above. Cells were imaged 72 h post-siRNA transfection. To check knockdown efficiency, U2OS cells were plated into 6-well dishes and reverse transfected with siRNA using RNAiMAX (Invitrogen) according to the manufacture's instructions. Cells were collected 72 h post transfection for western blot analysis.

Western blotting

All antibodies used for immunoblotting, immunoprecipitation and immunofluorescence are commercially available and were previously validated for the respected application. Cells were collected 72 h post siRNA transfection and lysed in Triton lysis buffer (1% Triton X-100, 100 mM NaCl and 50 mM Tris-HCl, pH 8.0, 5 mM $MgCl_2$, 0.1% Benzonase (Sigma Aldrich), 1x protease inhibitor (Roche)) on an orbital rotator at 4°C for 30 min. Lysates were centrifuged at 20 000 g for 15 min and supernatant was collected. Protein samples were quantified using Bradford (BioRad) and equal amounts of protein were loaded on gels for SDS-PAGE prior to western blotting. Samples were transferred to a PVDF membrane at 150 mA for 3 h, blocked with 5% milk in TBST (10 mM Tris–HCl, pH 7.6, 150 mM NaCl, 0.2% Tween-20) for 1 h and incubated in primary antibody in 1% milk in TBST (see list in TableS2), overnight at 4°C. Primary antibodies were detected using anti-mouse or anti-rabbit HRP antibodies (BioRad) in 1% milk in TBST. Membranes were visualised on Hyperfilm ECL films (Cytiva) and WesternBright ECL spray (Advansta).

Immunoprecipitation.

YFP-PARP1 expression was induced in U2OS Flp-In T-REx YFP-tagged-PARP1 WT cells by adding doxycycline (0.5 μg/mL) for 24 h before treatment. Cells were treated with Olaparib (30 μM) for 30 min before adding H_2O_2 (2 mM) for 15 min, or not when indicated before cell collection. Cells were harvested and washed twice with ice-cold phosphate-buffered saline (PBS) containing a protease inhibitor cocktail (Roche) before lysis in RIPA buffer supplemented with $MgCl_2$ (2.5 mM), EDTA (1 mM), 1x protease inhibitor, PMSF (1 mM) and Benzonase (50 u/mL). Ethidium bromide was added to lysates at a final 20 μg/mL concentration to disrupt potential DNA-dependent protein interactions (Lai et al., 1992). Samples were incubated on ice for 30 min with agitation every 5 min to aid lysis. Lysates were cleared by centrifugation at 20,000 x g for 20 min at 4°C, and the soluble fraction was collected. Lysates (1mg) were added to GFP-Trap agarose beads pre-equilibrated with dilution buffer (10 mM Tris-HCl pH 7.5, 150 mM NaCl, 0.5 mM EDTA) (Proteintech). Samples were incubated 2 h at 4°C with end-over-end rotation. Beads were washed thrice

with dilution buffer with 0.05% NP-40. Boiling beads for 5 min at 95°C in a 4X SDS sample buffer containing 50 mM DTT eluted immunoprecipitated proteins. Proteins were resolved by SDS-PAGE and transferred to nitrocellulose membrane. After 1 h blocking in 5% bovine serum albumin (BSA) TBS, membranes were incubated overnight at 4°C either with primary antibodies in 5% BSA TBS. Inputs represent 5% of lysate used for immunoprecipitation, and ponceau was used to assess the loading.

Immunofluorescence

Cells were washed once with PBS 1x before fixation with 3% paraformaldehyde for 10 min. Cells were then permeabilized with 0.5% Triton X-100 in PBS for 10 min, washed three times with PBS, and incubated in blocking buffer (3% BSA and 0.1% Triton X-100 in PBS) for 1 hour at room temperature (RT). Samples were incubated in primary antibody diluted in blocking buffer 1h at RT as listed in Table S2. Cells were washed thrice with 0.1% Triton X-100 in PBS before incubation with fluorescently tagged secondary antibody diluted in blocking buffer at RT for 1 hour in the dark. Cells were washed twice with 0.1% Triton X-100 in PBS and counterstained with Hoechst (1 µg/ml in PBS) for 10 min.

Confocal imaging after laser-induced DNA damage

For live-cell imaging combined with laser irradiation, a Ti-E inverted microscope (Nikon) equipped with a CSU-X1 spinning-disk head (Yokogawa) was used. The cells were imaged with a Plan APO 60×/1.4 NA oil-immersion objective lens and a sCMOS ORCA Flash 4.0 camera. The fluorescence of EGFP and the activated form of PAGFP was excited at 490 nm and detected with a bandpass filter at 500-550 nm. The fluorescence of TagRFP and the activated form of PATagRFP was excited at 561 nm and detected at 580-650 nm. Laser microirradiation and local H2B photoactivation at 405 nm was performed along a 16 µm-line through the nucleus using a single-point scanning head (iLas2 from Roper Scientific) coupled to the epifluorescence backboard of the microscope. To ensure reproducibility, laser power at 405 nm was measured at the beginning of each experiment and set to 125 µW at the sample level. Cells were maintained at 37◦C with a heating chamber in absence of CO_2. The same setup was used to image cells after immunostaining, with excitation at 405 nm and detection between 420 and 460 nm for imaging Hoechst, excitation at 490 nm and detection between 500 and 550 nm for imaging AF488 and excitation at 633 nm and detection over 650 nm for imaging AF647.

Image analysis

Quantification of fluorescence signal was performed with FIJI (https://fiji.sc/). For protein recruitment at DNA lesions, the images were first registered using the MultiStackReg plugin (Thevenaz et al., 1998), then regions of interest were delineated manually to measure the mean fluorescence intensity in the damaged region (I_d), in the whole nucleus (I_n) and in a background region outside of the cell (I_{bg}). Protein accumulation at sites of damage (A_d) was then calculated as:

$$A_d = \frac{I_d - I_{bg}}{I_n - I_{bg}}$$

The intensity within the microirradiated area was then normalized to the intensity prior to damage induction. The amount of mCherry-PARP1 accumulating at the LacO array (A_{lo}) was quantified with the following equation where I_o is the intensity of the LacO array, I_n is the mCherry signal in the nucleoplasm devoid of the LacO array and I_{bg} is the intensity of the background:

$$A_{lo} = \frac{I_o - I_{bg}}{I_n - I_{bg}}$$

The intensity within the LacO array was then normalized to the intensity prior to damage induction. Chromatin relaxation at DNA lesions was determined using a custom MATLAB routine that measures the changes in the thickness of the photoconverted H2B line relative to its value immediately after damage induction (Sellou et al., 2016).

Fluorescence correlation spectroscopy

Fluorescence Correlation Spectroscopy (FCS) experiments were performed on a Zeiss LSM880 confocal setup equipped with a C-Apo 40x/1.2 N.A. water immersion objective. GFP fluorescence was excited with a 488 nm laser and single emitted photons, selected by a bandpass filter at 500-550 nm, were detected and counted on a GaAsP spectral detector. Each FCS acquisition lasted 30 seconds and laser power was set to obtain optimal signal-to-noise ratios for the autocorrelation curves while minimizing photobleaching. Cells were maintained at 37°C with a heating chamber. Raw photon traces were detrended for slow fluctuations and correlated using the Fluctuation Analyzer 4G software (Wachsmuth et al., 2015).

Statistics and reproducibility

Data analysis and visualization was performed using R software (https://www.r-project.org/). The boxplot limits correspond to the 25th and 75th percentiles and the bold line indicates the median value. The whiskers extend 1.5 times the interquartile range. P values were calculated using an unpaired two-sided Student's t test, assuming unequal variances. For all data, we show a representative experiment among at least three independent repeats displaying consistent results. Blinding was not applied in the course of this study. Live-cell microscopy experiments aimed to acquire a minimum of 10 cells per condition to obtain normal distribution of the data and reliable means.

Reagent distribution

All reagents established during this study are available from the corresponding authors upon reasonable request.

ACKNOWLEDGMENTS

We thank the Microscopy-Rennes Imaging Center (BIOSIT, Université Rennes 1), member of the national infrastructure France-BioImaging supported by the French National Research Agency (ANR-10-INBS-04), for providing access to the imaging setups, as well as S. Dutertre and X. Pinson for technical assistance on the microscopes. We are grateful to K. Rippe and H. Lans for sharing reagents. For this work, the S.H.'s group received financial support from the Agence Nationale de la Recherche (PRC-2018 REPAIRCHROM), the Ligue contre le Cancer du Grand-Ouest (committees 22, 35, 53 and 72) and the Institut Universitaire de France. R.S. was supported by the Fondation ARC pour la recherche sur le cancer (PDF20181208405). The work in the Timinszky laboratory was supported by the Hungarian Academy of Sciences (LP2017-11/2017) and the National Research Development and Innovation Office (K128239). The collaboration between S.H. and G.T. benefited from funding from the partenariats Hubert Curien via the Balaton program.

REFERENCES

Aydin, ÖZ, Marteijn, JA, Ribeiro-Silva, C, Rodríguez López, A, Wijgers, N, Smeenk, G, van Attikum, H, Poot, RA, Vermeulen, W, and Lans, H (2014). Human ISWI complexes are targeted by SMARCA5 ATPase and SLIDE domains to help resolve lesion-stalled transcription. *Nucleic Acids Res* 42, 8473–8485.

Czarna, A, Berndt, A, Singh, HR, Grudziecki, A, Ladurner, AG, Timinszky, G, Kramer, A, and Wolf, E (2013). Structures of Drosophila cryptochrome and mouse cryptochrome1 provide insight into circadian function. *Cell* 153, 1394–1405.

Eberharter, A, Vetter, I, Ferreira, R, and Becker, PB (2004). ACF1 improves the effectiveness of nucleosome mobilization by ISWI through PHD-histone contacts. *EMBO J* 23, 4029–4039.

Erdel, F, Schubert, T, Marth, C, Längst, G, and Rippe, K (2010). Human ISWI chromatin-remodeling complexes sample nucleosomes via transient binding reactions and become immobilized at active sites. *Proc Natl Acad Sci* U S A 107, 19873–19878.
Fyodorov, DV, and Kadonaga, JT (2002). Binding of Acf1 to DNA involves a WAC motif and is important for ACF-mediated chromatin assembly. *Mol Cell Biol* 22, 6344–6353.

Gong, F et al. (2015). Screen identifies bromodomain protein ZMYND8 in chromatin recognition of transcription-associated DNA damage that promotes homologous recombination. *Genes Dev* 29, 197–211.

Grüne, T, Brzeski, J, Eberharter, A, Clapier, CR, Corona, DFV, Becker, PB, and Müller, CW (2003). Crystal structure and functional analysis of a nucleosome recognition module of the remodeling factor ISWI. *Mol Cell* 12, 449–460.

Ito, T, Levenstein, ME, Fyodorov, DV, Kutach, AK, Kobayashi, R, and Kadonaga, JT (1999). ACF consists of two subunits, Acf1 and ISWI, that function cooperatively in the ATP-dependent catalysis of chromatin assembly. *Genes Dev* 13, 1529–1539.

Izhar, L, Adamson, B, Ciccia, A, Lewis, J, Pontano-Vaites, L, Leng, Y, Liang, AC, Westbrook, TF, Harper, JW, and Elledge, SJ (2015). A Systematic Analysis of Factors

Localized to Damaged Chromatin Reveals PARP-Dependent Recruitment of Transcription Factors. *Cell Rep* 11, 1486–1500.

Juhász, S, Smith, R, Schauer, T, Spekhardt, D, Mamar, H, Zentout, S, Chapuis, C, Huet, S, and Timinszky, G (2020). The chromatin remodeler ALC1 underlies resistance to PARP inhibitor treatment. *Sci Adv* 6, eabb8626.

Klement, K, Luijsterburg, MS, Pinder, JB, Cena, CS, Del Nero, V, Wintersinger, CM, Dellaire, G, van Attikum, H, and Goodarzi, AA (2014). Opposing ISWI- and CHD-class chromatin remodeling activities orchestrate heterochromatic DNA repair. *J Cell Biol* 207, 717–733.

Kong, X, Mohanty, SK, Stephens, J, Heale, JT, Gomez-Godinez, V, Shi, LZ, Kim, J-S, Yokomori, K, and Berns, MW (2009). Comparative analysis of different laser systems to study cellular responses to DNA damage in mammalian cells. *Nucleic Acids Res* 37, e68.

Lai, J. S. & Herr, W. (1992) Ethidium bromide provides a simple tool for identifying genuine DNA-independent protein associations. *Proc. Natl. Acad. Sci.* 89, 6958–6962.

Lan, L et al. (2010). The ACF1 complex is required for DNA double-strand break repair in human cells. *Mol Cell* 40, 976–987.

Langelier, M-F, Planck, JL, Roy, S, and Pascal, JM (2012). Structural basis for DNA damage-dependent poly(ADP-ribosyl)ation by human PARP-1. *Science* 336, 728–732.

Leung, JWC et al. (2017). ZMYM3 regulates BRCA1 localization at damaged chromatin to promote DNA repair. *Genes Dev* 31, 260–274.

Liu, C, Vyas, A, Kassab, MA, Singh, AK, and Yu, X (2017). The role of poly ADP-ribosylation in the first wave of DNA damage response. *Nucleic Acids Research* 45, 8129.

Longarini, EJ et al. (2023). Modular antibodies reveal DNA damage-induced mono-ADP-ribosylation as a second wave of PARP1 signaling. *Mol Cell* 83, 1743-1760.e11.

Luger, K, Mäder, AW, Richmond, RK, Sargent, DF, and Richmond, TJ (1997). Crystal structure of the nucleosome core particle at 2.8 A resolution. *Nature* 389, 251–260.

Luijsterburg, MS et al. (2016). PARP1 Links CHD2-Mediated Chromatin Expansion and H3.3 Deposition to DNA Repair by Non-homologous End-Joining. *Mol Cell* 61, 547–562.

Oppikofer, M et al. (2017a). Non-canonical reader modules of BAZ1A promote recovery from DNA damage. *Nat Commun* 8, 862.

Oppikofer, M, Bai, T, Gan, Y, Haley, B, Liu, P, Sandoval, W, Ciferri, C, and Cochran, AG (2017b). Expansion of the ISWI chromatin remodeler family with new active complexes. *EMBO Rep* 18, 1697–1706.

Polo, SE, Kaidi, A, Baskcomb, L, Galanty, Y, and Jackson, SP (2010). Regulation of DNA-damage responses and cell-cycle progression by the chromatin remodelling factor CHD4. *EMBO J* 29, 3130–3139.

Prokhorova, E et al. (2021). Serine-linked PARP1 auto-modification controls PARP inhibitor response. *Nat Commun* 12, 4055.

Reyes, AA, Marcum, RD, and He, Y (2021). Structure and Function of Chromatin Remodelers. *J Mol Biol* 433, 166929.

Rother, MB et al. (2020). CHD7 and 53BP1 regulate distinct pathways for the re-ligation of DNA double-strand breaks. *Nat Commun* 11, 5775.

Sánchez-Molina, S, Mortusewicz, O, Bieber, B, Auer, S, Eckey, M, Leonhardt, H, Friedl, AA, and Becker, PB (2011). Role for hACF1 in the G2/M damage checkpoint. *Nucleic Acids Res* 39, 8445–8456.

Sellou, H et al. (2016). The poly(ADP-ribose)-dependent chromatin remodeler Alc1 induces local chromatin relaxation upon DNA damage. *Mol Biol Cell* 27, 3791–3799.

Sexton, T, and Cavalli, G (2015). The role of chromosome domains in shaping the functional genome. *Cell* 160, 1049–1059.

Singh, HR et al. (2017). A Poly-ADP-Ribose Trigger Releases the Auto-Inhibition of a Chromatin Remodeling Oncogene. *Mol Cell* 68, 860-871.e7.

Singh, JK et al. (2021). Zinc finger protein ZNF384 is an adaptor of Ku to DNA during classical non-homologous end-joining. *Nat Commun* 12, 6560.

Smeenk, G et al. (2013). Poly(ADP-ribosyl)ation links the chromatin remodeler SMARCA5/SNF2H to RNF168-dependent DNA damage signaling. *J Cell Sci* 126, 889–903.

Smith, R et al. (2023). HPF1-dependent histone ADP-ribosylation triggers chromatin relaxation to promote the recruitment of repair factors at sites of DNA damage. *Nat Struct Mol Biol* 30, 678-691.

Smith, R, Lebeaupin, T, Juhász, S, Chapuis, C, D'Augustin, O, Dutertre, S, Burkovics, P, Biertümpfel, C, Timinszky, G, and Huet, S (2019). Poly(ADP-ribose)-dependent chromatin unfolding facilitates the association of DNA-binding proteins with DNA at sites of damage. *Nucleic Acids Res* 47, 11250–11267.

Smith, R, Sellou, H, Chapuis, C, Huet, S, and Timinszky, G (2018). CHD3 and CHD4 recruitment and chromatin remodeling activity at DNA breaks is promoted by early poly(ADP-ribose)-dependent chromatin relaxation. *Nucleic Acids Res* 46, 6087–6098.

Suskiewicz, MJ et al. (2023). Updated protein domain annotation of the PARP protein family sheds new light on biological function. *Nucleic Acids Res*, gkad514.

Tessarz, P, and Kouzarides, T (2014). Histone core modifications regulating nucleosome structure and dynamics. *Nat Rev Mol Cell Biol* 15, 703–708.

Thévenaz, P, Ruttimann, UE, and Unser, M (1998). A pyramid approach to subpixel registration based on intensity. *IEEE Trans Image Process* 7, 27–41.

Timinszky, G et al. (2009). A macrodomain-containing histone rearranges chromatin upon sensing PARP1 activation. *Nat Struct Mol Biol* 16, 923–929.

Wachsmuth, M, Conrad, C, Bulkescher, J, Koch, B, Mahen, R, Isokane, M, Pepperkok, R, and Ellenberg, J (2015). High-throughput fluorescence correlation spectroscopy enables analysis of proteome dynamics in living cells. *Nat Biotech* 33, 384–389.

Xu, Y, Sun, Y, Jiang, X, Ayrapetov, MK, Moskwa, P, Yang, S, Weinstock, DM, and Price, BD (2010). The p400 ATPase regulates nucleosome stability and chromatin ubiquitination during DNA repair. *J Cell Biol* 191, 31–43.

Zhang, Y et al. (2011). RNF146 is a poly(ADP-ribose)-directed E3 ligase that regulates axin degradation and Wnt signalling. *Nat Cell Biol* 13, 623–629.

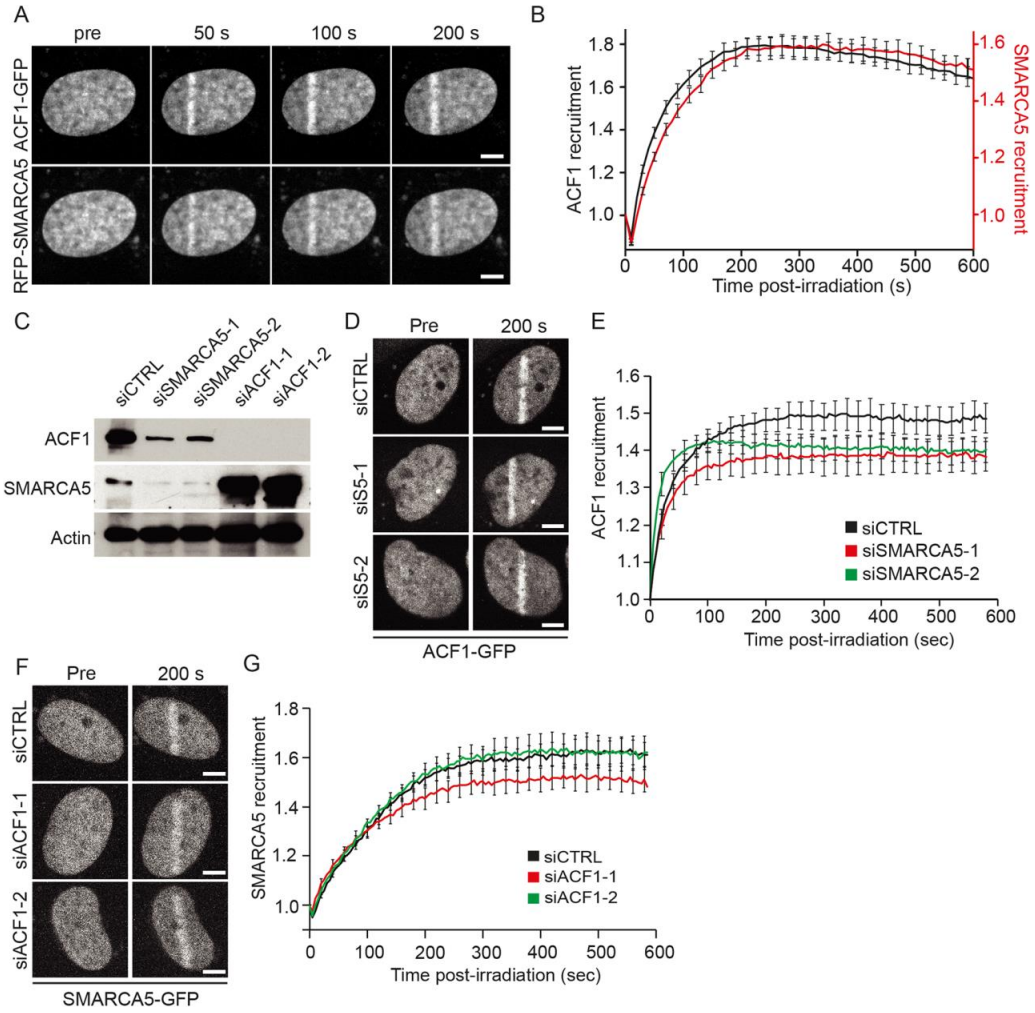

FIGURE LEGENDS

Figure 1. ACF1 and SMARCA5 accumulate to DNA lesions independently of each other. (A-B) Images (A) and kinetics (B) of ACF1-GFP and TagRFP-SMARCA5 recruitment to sites of DNA damage induced by 405 nm laser irradiation. The two constructs were co-expressed in U2OS cells. Curves are mean±SEM of 14 cells. (C) Western blot showing knockdown efficiency of SMARCA5 (siSMARCA5-1, siSMARCA-2) or ACF1 (siACF1-1, siACF1-2) as compared to scrambled siRNA (siCTRL). Actin was used as loading control. (D-E) Images (D) and kinetics (E) of ACF1-GFP recruitment to sites of DNA damage induced by 405 nm laser irradiation in U2OS cells knocked-down for SMARCA5 (siS5-1, siS5-2) or treated with scrambled siRNA (siCTRL). Curves are mean±SEM of 10-15 cells per condition. (F-G) Images (F) and kinetics (G) of SMARCA5-GFP recruitment to sites of DNA damage induced by 405 nm laser irradiation in U2OS cells knocked-down for ACF1 (siACF1-1, siACF1-2) or treated with scrambled siRNA (siCTRL). Curves are mean±SEM of 11-16 cells per condition. For A, D and F, scale bars, 5 µm.

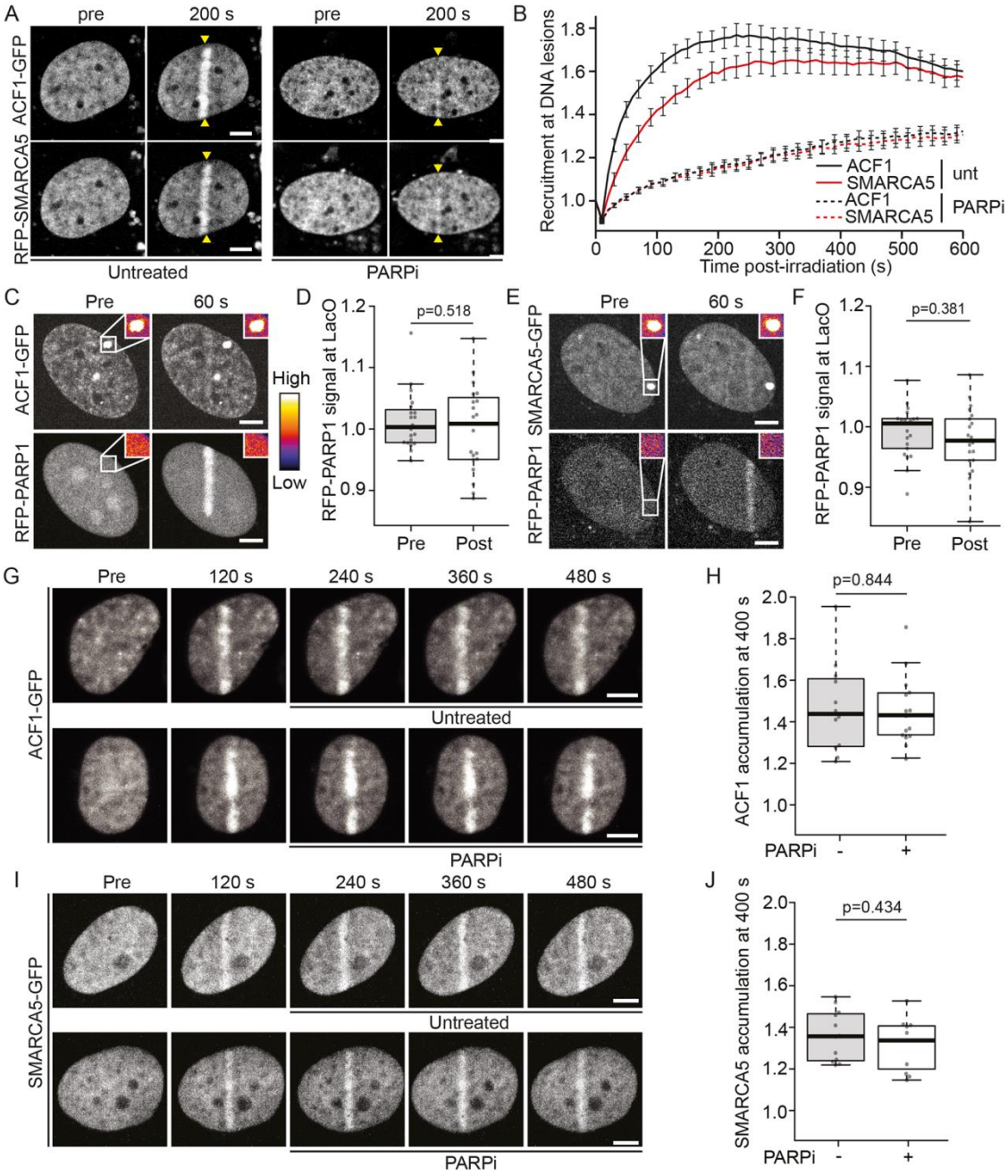

Figure 2. The ADP-ribosylation dependent recruitment of ACF1 and SMARCA5 to DNA lesions is not due to direct binding to ADP-ribose. (A-B) Images (A) and kinetics (B) of ACF1-GFP and TagRFP-SMARCA5 recruitment to sites of DNA damage induced by 405 nm laser irradiation in U2OS cells treated or not with 30 µM of the PARP inhibitor Olaparib (PARPi). The yellow arrowheads indicate the position of the irradiated line. Curves are mean±SEM of 14 cells. (C) ACF1-GFP tethered to the LacO array is unable to recruit ADP-ribosylated mCherry-PARP1 after DNA damage induction. Insets, pseudocolored according to the look-up table displayed on the right, show magnification of the LacO array. (D) Boxplots show mCherry-PARP1 intensity at the LacO array tethering ACF1-GFP. The average intensity at the spot is quantified pre and 60 s post damage, corrected for background

and normalized to average intensity of the nucleus. 20 cells per condition. (E) SMARCA5-GFP tethered to the LacO array cannot recruit ADP-ribosylated mCherry-PARP1 after DNA damage induction. Insets, pseudocolored according to the look-up table on the left of panel C, show magnifications of the LacO array. (F) Boxplots show mCherry-PARP1 intensity at the LacO array tethering SMARCA5-GFP. The average intensity at the spot is quantified pre and 60 s post damage, corrected for background and normalized to average intensity of the nucleus. 20 cells per condition. (G-H) Images (G) and quantification (H) of ACF1-GFP accumulation at sites of DNA damage in cells were left untreated or treated with 30 µM Olaparib (PARPi) 180 s after DNA damage induction. Protein accumulation was quantified 400 s after irradiation for 12-15 cells per condition. (I-J) Images (I) and quantification (J) of SMARCA5-GFP accumulation at sites of DNA damage in cells were left untreated or treated with 30 µM Olaparib (PARPi) 180 s after DNA damage induction. Protein accumulation was quantified 400 s after irradiation for 11-12 cells per condition. For A, C, E, G and I, scale bars, 5 µm.

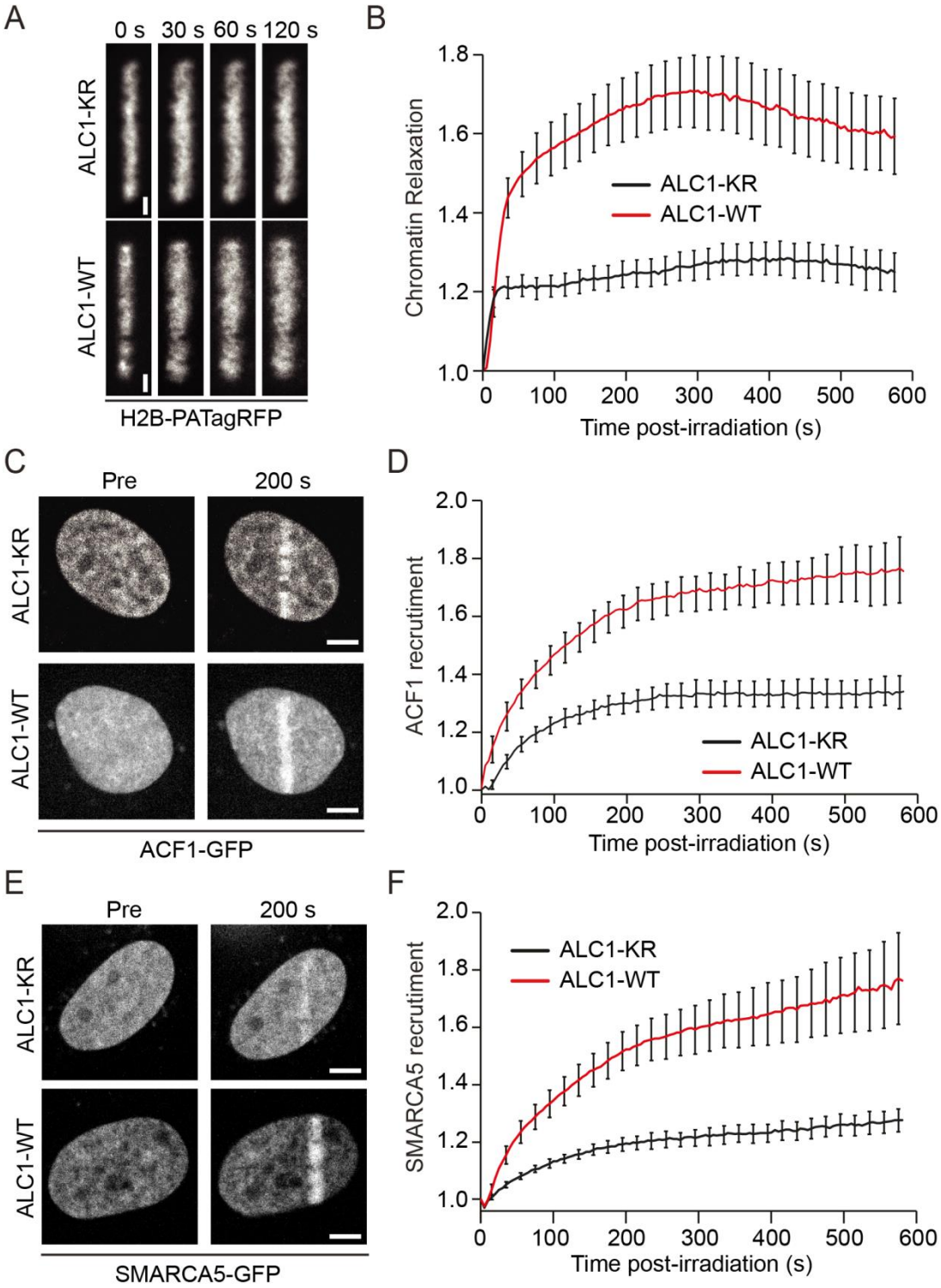

Figure 3. The accumulation of ACF1 and SMARCA5 to DNA lesions is promoted by ADP-ribosylation dependent chromatin unfolding. (A) Image sequences of the chromatin line area which is simultaneously damaged and photoconverted by irradiation at 405 nm in U2OS cells co-expressing H2B-PATagRFP and iRFP670 tagged wild-type ALC1 or the catalytically-dead mutant ALC1-K77R. Scale bars, 2 µm. The broadening of the photoconverted line is the consequence of chromatin relaxation upon damage induction. (B) Kinetics of chromatin

relaxation in U2OS cells co-expressing H2B-PATagRFP and iRFP670 tagged wild-type ALC1 or ALC1-K77R. Curves are mean±SEM of 14-16 cells per condition. (C-D) Images (C) and kinetics (D) of ACF1-GFP recruitment to sites of DNA damage induced by 405 nm laser irradiation in U2OS cells co-expressing mCherry tagged wild-type ALC1 or ALC1-K77R. Curves are mean±SEM of 10-15 cells per condition. (E-F) Images (E) and kinetics (F) of SMARCA5-GFP recruitment to sites of DNA damage induced by 405 nm laser irradiation in U2OS cells co-expressing iRFP670 tagged wild-type ALC1 or ALC1-K77R. Curves are mean±SEM of 12 cells per condition. For C and E, scale bars, 5 μm.

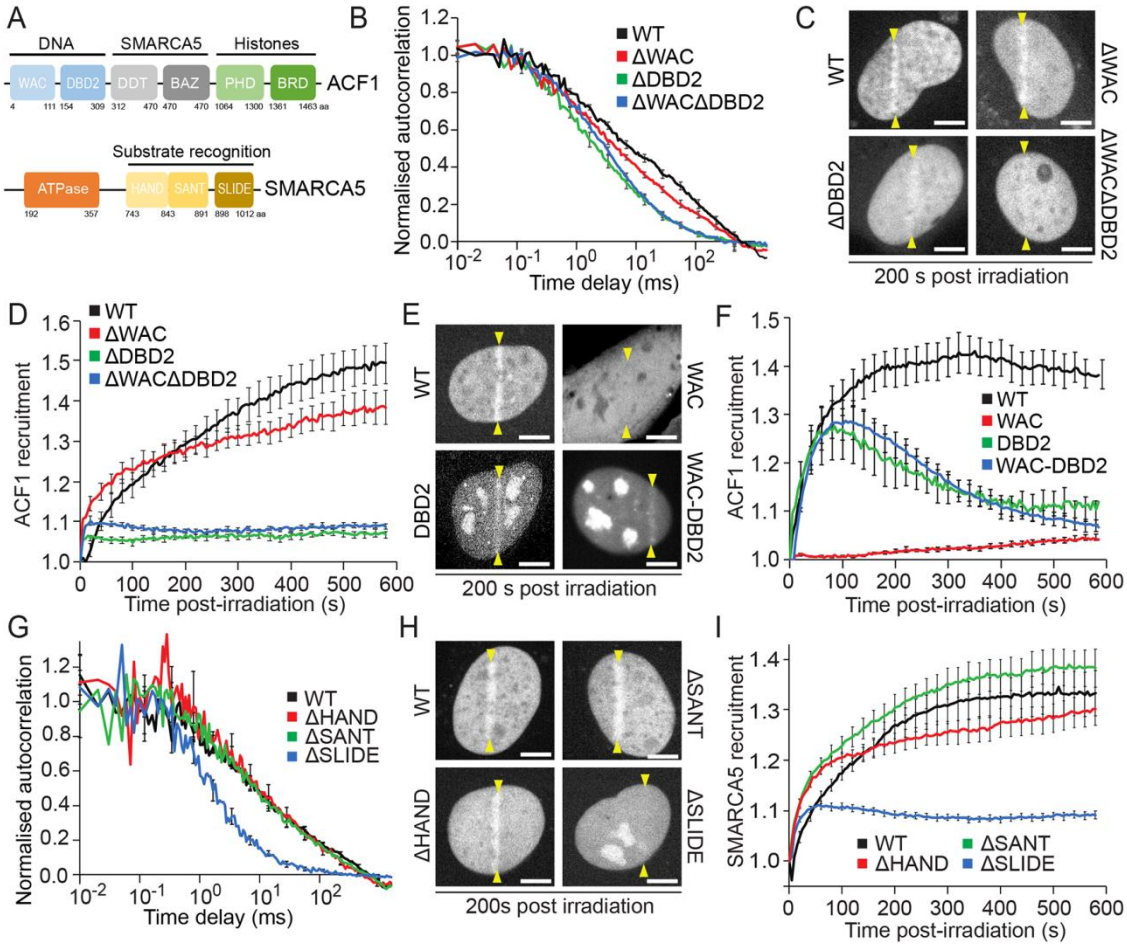

Figure 4. The accumulation of ACF1 and SMARCA5 to sites of damage is driven by DNA binding. (A) Sketch of the different domains of ACF1 and SMARCA5 and their binding substrates (B) Normalized FCS correlation curves were obtained in undamaged U2OS nuclei expressing GFP-tagged wild-type ACF1 or mutants lacking either the WAC domain, the DBD2 domain, or both domains. Curves are mean±SEM of 10 cells per condition. (C-D) Images (C) and kinetics (D) of the recruitment to sites of damage of GFP-tagged wild-type ACF1 or mutants lacking either the WAC domain, the DBD2 domain or both domains. Curves are mean±SEM of 11-13 cells per condition. (E-F) Images (E) and kinetics (F) of the recruitment to sites of damage of wild-type ACF1, the WAC domain, the DBD2 domain or a construct comprising both domains, all tagged with GFP. Curves are mean±SEM of 11-14 cells per condition. (G) Normalized FCS correlation curves obtained in undamaged U2OS nuclei expressing GFP-tagged wild-type SMARCA5 or mutants lacking either the HAND, SANT or SLIDE domains. Curves are mean±SEM of 12 cells per condition. (H-I) Images (H) and kinetics (I) of the recruitment to sites of damage of GFP-tagged wild-type SMARCA5 or mutants lacking either the HAND, SANT or SLIDE domains. Curves are mean±SEM of 12-13 cells per condition. For C, E and H, scale bars, 5 µm.

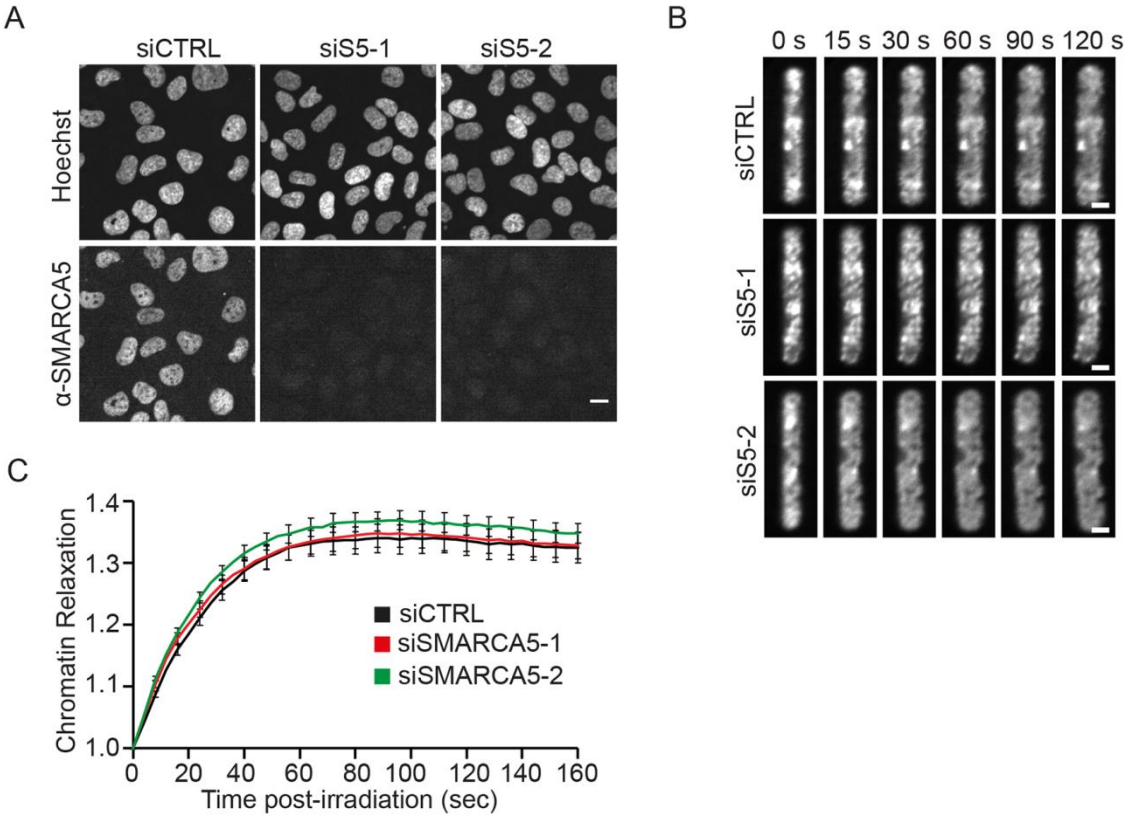

Figure 5. The ACF complex does not contribute to early chromatin unfolding at DNA lesions. (A) Immunofluorescence of U2OS cells treated with negative control siRNA (siCTRL) or siRNAs against SMARCA5 (siS5-1/2) and stained with Hoechst and an antibody targeting SMARCA5. Scale bar, 10 µm. (B-C) Confocal image sequences (B) and kinetics of relaxation (C) of the chromatin line in U2OS expressing H2B-PAGFP and treated with control siRNA or siRNAs against SMARCA5. Scale bars, 2 µm. Curves are mean±SEM of 19-20 cells per condition.